Available online at www.sciencedirect.com

ScienceDirect

Journal of Ocean Engineering and Science 2 (2017) 253–267

www.elsevier.com/locate/joes

# A framework for efficient irregular wave simulations using Higher Order Spectral method coupled with viscous two phase model

Inno Gatin[a,*], Vuko Vukčević[a], Hrvoje Jasak[a,b]

[a] *Faculty of Mechanical Engineering and Naval Architecture, University of Zagreb, Ivana Lučića 5, Zagreb, Croatia*
[b] *Wikki Ltd., 459 Southbank House, SE1 7SJ London, United Kingdom*

Received 10 May 2017; received in revised form 24 July 2017; accepted 6 September 2017
Available online 14 September 2017

**Abstract**

In this paper a framework for efficient irregular wave simulations using Higher Order Spectral method coupled with fully nonlinear viscous, two-phase Computational Fluid Dynamics (CFD) model is presented. CFD model is based on solution decomposition via Spectral Wave Explicit Navier–Stokes Equation method, allowing efficient coupling with arbitrary potential flow solutions. Higher Order Spectrum is a pseudo-spectral, potential flow method for solving nonlinear free surface boundary conditions up to an arbitrary order of nonlinearity. It is capable of efficient long time nonlinear propagation of arbitrary input wave spectra, which can be used to obtain realistic extreme waves. To facilitate the coupling strategy, Higher Order Spectrum method is implemented in foam-extend alongside the CFD model. Validation of the Higher Order Spectrum method is performed on three test cases including monochromatic and irregular wave fields. Additionally, the coupling between Higher Order Spectrum and CFD is validated on three hour irregular wave propagation. Finally, a simulation of a 3D extreme wave encountering a full scale container ship is shown.


*Keywords:* Higher Order Spectral method; Irregular waves; Extreme waves; CFD; Foam-extend.

## 1. Introduction

With increased availability of CPU resources during past few decades, Computational Fluid Dynamics (CFD) is becoming a standard practice for simulation of transient free-surface waves. CFD methods that model fully-nonlinear, two-phase, viscous flow exhibit high computational costs, which prohibit long time wave evolution in a large domain. This disadvantage is partially overcome using domain decomposition strategies, where the flow in a small, relevant part of the domain is resolved using CFD, while the farfield flow is resolved using potential flow, a computationally cheaper model. Given the potential flow solution, the CFD simulation naturally develops nonlinear, viscous flow with vorticity effects. First decomposition method was developed by Van Dalsem and Steger [1], called Fortified Navier–Stokes (FNS) method. Van Dalsem and Steger used the decomposition to 'fortify' the solution of subset equations in the boundary layer, while solving ordinary Navier–Stokes in the rest of the domain. Jacobsen et al. [2] introduced a domain decomposition method for wave modelling using relaxation zones. Paulsen et al. [3] used one-way coupling between fully nonlinear potential flow solver (developed by Ensig-Karup et al. [4]) and fully nonlinear viscous CFD solver to investigate wave loads on a circular surface piercing cylinder. The same method was used to calculate steep regular wave loads on a bottom mounted cylinder [5]. Pistidda and Ottens [6] used the Euler Overlay Method for domain decomposition to calculate the Response Amplitude Operator (RAO) for a moonpool of a deep water construction vessel.

Vukčević and Jasak [7] developed a modified Spectral Wave Explicit Navier–Stokes Equation (SWENSE) [8–10] solution decomposition method which is used alongside domain decomposition. The solution is decomposed into incident and

* Corresponding author.
*E-mail addresses:* inno.gatin@fsb.hr, innogatin@gmail.com (I. Gatin), vuko.vukcevic@fsb.hr (V. Vukčević), h.jasak@wikki.co.uk, hrvoje.jasak@fsb.hr (H. Jasak).

http://dx.doi.org/10.1016/j.joes.2017.09.003

diffracted fields, where the incident field is obtained from the potential flow model, while the diffracted field is solved via two-phase, viscous CFD model. All of the above mentioned CFD methods are computationally expensive because they are modelling highly resolved spatial flow features with nonlinear and coupled equations in time domain. Hence, they cannot be used to perform a large number of long time irregular wave field propagations needed to obtain a naturally emerging extreme wave.

Extreme wave loads are gaining more attention due to increasing number of offshore objects being installed worldwide. Extreme waves emerge due to focusing of wave spectrum components, which is influenced by nonlinear wave modulation and wave-to-wave interaction. It is considered that the influence of wind and atmospheric pressure, bathymetry and current [11] also plays a role in extreme wave generation. Apart from the focusing of unidirectional spectrum, geometric focusing of directional spectrum can also cause extreme wave events.

Assessment of extreme wave loads demands accurate wave modelling. Since extreme waves occur randomly in an irregular sea state, in order to obtain a statistically and physically accurate extreme wave, irregular sea state needs to be evolved for a long time on a large domain. Moreover, the evolution of the irregular sea state has to take into account nonlinear effects of wave interaction and modulation. CFD takes into account all nonlinearities of the flow, and inherently the nonlinearities of wave-to-wave interaction and wave modulation. However, even with domain decomposition methods, it is challenging to propagate arbitrary wave field for a sufficient amount of time to observe a natural emergence of extreme waves. Apart from that, long time CFD simulation might accumulate discretization errors which will inevitably influence the wave field. To obtain a realistic extreme wave in an irregular sea state, as much as a thousand peak periods need to be simulated. Paulsen et al. [3] reported that one irregular wave peak period took 8 hours to compute on 10 CPU's, extrapolating to almost a year for 1000 peak periods, which might be necessary to obtain a realistic extreme wave.

Nonlinear wave field can be efficiently propagated using spectral potential flow approach. In this work, potential flow pseudo-spectral Higher Order Spectral (HOS) method is used. Nonlinearities of wave-to-wave interaction and wave modulation are taken into account, while viscous effects, vorticity, wave breaking, diffraction and radiation are neglected. Since the latter effects have minor influence on extreme wave emergence, HOS method can be used to perform a long time evolution of an irregular wave field on a large-scale domain to obtain a statistically and physically consistent extreme wave. HOS can then be coupled with CFD in a small spatial domain containing the extreme wave, and for a short period of time to capture viscous effects, wave breaking and fluid–structure interaction. In this work one-way coupling between HOS and CFD is achieved using the decomposition model [7].

HOS method was first developed by Dommermuth and Yue [12] and West et al. [13] independently. West et al. used order consistent Taylor and perturbation series expansion, which is adopted by most HOS algorithms today [14,15]. Since the publication of the original method in 1987, numerous authors continued its development. Ducrozet et al. [15] enhanced numerical efficiency and aliasing treatment, while Tanaka [14] combined HOS with complex amplitude function. Dommermuth [16] developed a time relaxation scheme which enables HOS calculation to be initialized with a linear solution. This is of crucial importance since wave energy spectra are defined for linear wave components.

In this paper a mathematical overview of the HOS method is given, followed by a detailed description of numerical procedure. The CFD model and coupling with potential flow by Vukčević and Jasak [7] is used. Three test cases are considered for HOS validation purposes. The first case considers monochromatic wave train propagation, where modal amplitudes are compared with analytical Stokes solution. Second test case considers propagation of four uniformly steep spectra, where the HOS solution is compared to viscous, two-phase CFD solution. Third test case shows naturally occurring Benjamin–Feir instabilities [17]. In addition to the validation of the implemented HOS model, the coupling between HOS and CFD using SWENSE is also validated on a three hour irregular wave propagation case. Finally, an example simulation of a 3D extreme wave encountering a full scale container ship is shown. According to ITTC guidelines, the present method applied on this case presents a fully-nonlinear seakeeping calculation.

## 2. Mathematical model

In this section mathematical model for the HOS method is outlined; the reader is referred to [12–15] for more details.

Pseudo-spectral HOS method is used to reformulate nonlinear partial differential equation set via perturbation, Taylor and Fourier series into a set of ordinary differential equations.

### 2.1. Governing equations

In this model, free-surface flow is assumed irrotational, inviscid and incompressible. Surface gravity wave propagation is described with the following governing equations:

- Laplace equation for incompressible, irrotational, inviscid flow:

$$\nabla^2\phi(x, y, z, t) = 0, \tag{1}$$

where $\phi$ is the velocity potential, while $x$, $y$, $z$ are spatial coordinates and $t$ is time.

- Dynamic free surface boundary condition:

$$\frac{\partial\phi}{\partial t} + gz + \frac{1}{2}(\nabla\phi)^2 = 0, \tag{2}$$

where $g$ is the gravitational acceleration in the direction of negative $z$ axis.

- Kinematic free surface boundary condition:

$$\frac{\partial\eta}{\partial t} + \left(\frac{\partial\phi}{\partial x}, \frac{\partial\phi}{\partial y}\right) \cdot \left(\frac{\partial\eta}{\partial x}, \frac{\partial\eta}{\partial y}\right) = \frac{\partial\phi}{\partial z}, \tag{3}$$

where $\eta = \eta(x, y, t)$ is a single valued function of the free surface displacement.

Depth is considered uniform and the bottom impermeable, while the domain is assumed periodic in the horizontal directions [15].

Eqs. (2) and (3) can be rewritten in terms of surface potential $\psi(x, y, t) = \phi(x, y, \eta(x, y, t), t)$, as they are valid for $z = \eta(x, y, t)$:

$$\frac{\partial \psi}{\partial t} + g\eta + \frac{1}{2}\left(\frac{\partial \psi}{\partial x}, \frac{\partial \psi}{\partial y}\right)^2 - \frac{1}{2}\left(\frac{\partial \phi}{\partial z}\bigg|_{z=\eta}\right)^2 \left(1 + \left(\frac{\partial \eta}{\partial x}, \frac{\partial \eta}{\partial y}\right)^2\right) = 0, \tag{4}$$

$$\frac{\partial \eta}{\partial t} + \left(\frac{\partial \psi}{\partial x}, \frac{\partial \psi}{\partial y}\right) \cdot \left(\frac{\partial \eta}{\partial x}, \frac{\partial \eta}{\partial y}\right) - \frac{\partial \phi}{\partial z}\bigg|_{z=\eta} \left(1 + \left(\frac{\partial \eta}{\partial x}, \frac{\partial \eta}{\partial y}\right)^2\right) = 0. \tag{5}$$

### 2.2. Higher Order Spectral method

A pseudo-spectral, HOS method has been used to obtain a nonlinear solution of free surface boundary conditions, Eqs. (4) and (5). All spatial derivatives are evaluated in wave number space, while time derivatives are evolved in physical space instead of the frequency domain. The shape function for velocity potential used in the wave number space is:

$$\phi(x, y, z, t) = \sum_k \sum_l c_{k,l}(t) \frac{\cosh\left(K_{k,l}(z + d)\right)}{\cosh(K_{k,l} d)} e^{iK_k x} e^{iK_l y}, \tag{6}$$

where $c_{k,l}(t)$ are the time-dependent Fourier coefficients, while $K_{k,l}$, $K_k$ and $K_l$ are wave numbers defined as:

$$K_k = \frac{2\pi k}{L_x}, \tag{7}$$

$$K_l = \frac{2\pi l}{L_y}, \tag{8}$$

$$K_{k,l} = \sqrt{K_k^2 + K_l^2}. \tag{9}$$

Fourier series decomposition given by Eq. (6) allows us to calculate horizontal derivatives analytically, whereas vertical derivative needs special treatment as it represents vertical velocity of the free surface $W$, at the unknown wave elevation $\eta$. Hence, it is necessary to use the full form of the shape function given by Eq. (6), calculate its derivative it in $z$ direction, and evaluate it at the exact free surface location. This presents a Dirichlet problem for the velocity potential $\phi$ on a boundary of complicated shape $\eta(x, y, t)$. In order to circumvent this difficulty, the surface potential is expanded in a Taylor series around $z = 0$ in terms of $\eta$:

$$\phi(x, y, \eta, t) = \psi(x, y, t) = \sum_{i=0}^{\infty} \frac{\eta^i}{i!} \frac{\partial^i}{\partial z^i} \phi(x, y, 0, t). \tag{10}$$

The vertical derivative of surface potential is:

$$W(x, y, t) = \frac{\partial \phi}{\partial z}\bigg|_{z=\eta} = \sum_{i=0}^{\infty} \frac{\eta^i}{i!} \frac{\partial^{i+1}}{\partial z^{i+1}} \phi(x, y, 0, t). \tag{11}$$

To keep the solution up to an arbitrary order of nonlinearity, the potential is expanded in perturbation series in terms of wave slope $\epsilon = Ka$, where $K$ is the wave number and $a$ is the wave amplitude:

$$\phi(x, y, z, t) = \phi_1 + \epsilon\phi_2 + \epsilon^2\phi_3 + \cdots = \sum_{m=1}^{M} \phi^{(m)}, \tag{12}$$

where $M$ is the perturbation series order of nonlinearity. With every order of $\phi$ expanded in a Taylor series using Eq. (10), surface potential can be written as:

$$\psi(x, y, t) = \sum_{m=1}^{M} \sum_{i=0}^{M-m} \frac{\eta^i}{i!} \frac{\partial^i}{\partial z^i} \phi^{(m)}(x, y, 0, t). \tag{13}$$

The orders of nonlinearities are determined with respect to the product of $\eta^i$ and $\partial^i \phi^{(m)}/\partial z^i$, and the second sum in Eq. (13) is truncated at $M - m$ to account for order consistency. The unknowns in Eq. (13) are the individual orders of velocity potential $\phi^{(m)}$, which are calculated sequentially by equating the terms of the same order:

$$\phi^{(1)} = \psi(x, y, t),$$

$$\phi^{(2)} = -\eta \frac{\partial}{\partial z} \phi^{(1)},$$

$$\vdots$$

$$\phi^{(m)} = -\sum_{i=1}^{m-1} \frac{\eta^i}{i!} \frac{\partial^i}{\partial z^i} \phi^{(m-i)}; \quad m = 2, 3 \ldots, M. \tag{14}$$

Once the individual orders of $\phi$ are obtained, vertical velocity $W$ can be evaluated. Vertical velocity of the free surface is also expanded in a perturbation series, while the individual orders are calculated using orders of $\phi$ as follows:

$$W^{(m)} = \sum_{i=0}^{m-1} \frac{\eta^i}{i!} \frac{\partial^{(i+1)}}{\partial z^{(i+1)}} \phi^{(m-i)}; \quad m = 1, 2, \ldots, M. \tag{15}$$

Total vertical velocity is then obtained by summing all individual orders:

$$W(x, y, t) = \sum_{m=1}^{M} W^{(m)}. \tag{16}$$

In theory, the order of nonlinearity $M$ at which the expansion is truncated is arbitrary. The main advantage of this approach is that no iterations are needed per time step to resolve the coupling of the boundary conditions. Furthermore, Fourier transform facilitates the calculation of spatial derivatives, accelerating the numerical procedure.

## 3. Numerical model

The Fast Fourier Transform (FFT) algorithm is used for efficient calculation of the Fourier transform, while the fifth-order Cash–Karp embedded Runge–Kutta scheme with error

control and adjustable time-step size [18] is used to solve ordinary differential equations. In this section, emphasis is given on numerical procedure and initialisation of HOS calculation. Dealiasing, time integration and coupling with CFD are also briefly explained.

### 3.1. Numerical procedure

The numerical procedure starts with a discrete surface potential $\psi$ and surface elevation $\eta$ which are obtained from the previous time step or initial conditions. The discrete values are located on a uniform discrete mesh with nodes equidistantly spaced along the domain's length $L_x$ and width $L_y$. Hence, the mesh is fully defined with a number of nodes $N_x$ in $x$ and $N_y$ in $y$ direction, yielding mesh resolution $\Delta x = L_x/N_X$ and $\Delta y = L_y/N_y$. Using Eq. (6), the vertical derivative of velocity potential can generally be written as:

$$\frac{\partial^j \phi}{\partial z^j} = \frac{\partial^j}{\partial z^j}\left(\sum_k\sum_l c_{k,l}(t)\frac{\cosh\left(K_{k,l}(z+d)\right)}{\cosh(K_{k,l}d)}\,e^{iK_k x}\,e^{iK_l y}\right)$$
$$= \sum_k\sum_l c_{k,l}(t)\,K_{k,l}^j\,\frac{\sinh\left(K_{k,l}(z+d)\right)}{\cosh(K_{k,l}d)}\,e^{iK_k x}\,e^{iK_l y}. \quad (17)$$

While calculating individual terms of a given order in Eq. (14), the spatial derivatives are calculated in wave number space. After evaluating each order $\phi^{(m)}$ in physical space, it is transformed via FFT into wave number space. This is required in order to efficiently calculate vertical derivative of $\phi^{(m)}$, used in calculation of $\phi^{(m+1)}$. Once the individual derivatives are calculated, they are inversely transformed back into physical space before multiplying with a corresponding power of $\eta$. In the following equations, Fourier transform of a discrete field $f$ is denoted with $\mathscr{F}(f)$, and the inverse transform is denoted with $\mathscr{F}^{-1}(f)$. Eq. (14) can be written as:

$$\phi^{(1)} = \psi(x_n,t),$$
$$\phi^{(m)} = -\sum_{j=1}^{m-1}\frac{\eta^j}{j!}\,\mathscr{F}^{-1}\left\{\sum_k\sum_l c_{k,l}^{(m-j)}(t)\,K_{k,l}^j\,e^{iK_k x}\,e^{iK_l y}\right\};$$
$$m = 2,3,\ldots,M, \quad (18)$$

where $c_{k,l}^{(m-j)}(t)$ is the Fourier coefficient of order $m-j$ of the $k$, $l$th Fourier mode. It is calculated by performing FFT on preceding orders of $\phi$ on a discrete spatial mesh:

$$c_{k,l}^{(m-j)}(t) = \mathscr{F}\left\{\phi^{(m-j)}(x,y,t)\right\}. \quad (19)$$

Once all the orders of $\phi$ are evaluated, orders of vertical velocity $W$ are calculated using Eq. (15):

$$W^{(1)} = \mathscr{F}^{-1}\left\{\sum_k\sum_l c_{k,l}^{(1)}(t)\,K_{k,l}\,e^{iK_k x}\,e^{iK_l y}\right\},$$
$$W^{(m)} = \sum_{j=0}^{m-1}\frac{\eta^j}{j!}\,\mathscr{F}^{-1}\left\{\sum_k\sum_l c_{k,l}^{(m-j)}(t)\,K_{k,l}^{(j+1)}\,e^{iK_k x}\,e^{iK_l y}\right\};$$
$$m = 1,2,\ldots,M. \quad (20)$$

The inverse Fourier transforms occurring in Eq. (20) are already calculated in Eq. (18), except for the last order of vertical velocity $W^{(M)}$, for which the inverse Fourier transform has to be calculated separately. The inverse Fourier transforms calculated in Eq. (18) are hence stored for efficiency.

Once $\phi$, $\eta$ and $W$ are known, we proceed by evaluating the coupling terms in Eqs. (4) and (5). Spatial horizontal derivatives are calculated in the wave number space, hence the surface elevation displacement $\eta$ (available on discrete spatial mesh) has to be transformed via FFT. When all the derivatives are calculated, they are transformed back to the physical space and multiplied. Time marching boundary condition equations, Eqs. (4) and (5) can finally be written as:

$$\frac{\partial\psi(x,y,t)}{\partial t} = -g\,\eta(x,y,t)$$
$$-\frac{1}{2}\left(\mathscr{F}^{-1}\left\{\sum_k\sum_l c_{k,l}^{\psi}(t)\,iK_{k,l}\,e^{iK_k x}\,e^{iK_l y}\right\}\right)^2$$
$$+\frac{1}{2}W^2\left(1+\left(\mathscr{F}^{-1}\left\{\sum_k\sum_l c_{k,l}^{\eta}(t)\,iK_{k,l}\,e^{iK_k x}e^{iK_l y}\right\}\right)^2\right), \quad (21)$$

$$\frac{\partial\eta(x,y,t)}{\partial t} = W\left(1+\left(\mathscr{F}^{-1}\left\{\sum_k\sum_l c_{k,l}^{\eta}(t)\,iK_{k,l}\,e^{iK_k x}e^{iK_l y}\right\}\right)^2\right)$$
$$-\mathscr{F}^{-1}\left\{\sum_k\sum_l c_{k,l}^{\psi}(t)\,iK_{k,l}\,e^{iK_k x}e^{iK_l y}\right\}$$
$$\times\,\mathscr{F}^{-1}\left\{\sum_k\sum_l c_{k,l}^{\eta}(t)\,iK_{k,l}\,e^{iK_k x}e^{iK_l y}\right\}, \quad (22)$$

where $c_{k,l}^{\psi}(t)$ and $c_{k,l}^{\eta}(t)$ are the Fourier coefficients obtained by performing a Fourier transform on discrete values of $\psi$ and $\eta$, respectively. Fig. 1 shows the flow chart of the HOS method during one time step.

### 3.2. Time integration

Time integration of Eqs. (21) and (22) is performed with the fifth-order Cash–Karp embedded Runge–Kutta scheme with error control and adjustable time-step size. For more details on time integration the reader is referred to Press et al. [18].

### 3.3. Initialization of the wave field in a HOS simulation

In order to initialize a HOS simulation, discrete values of $\psi(x,y,t=0)$ and $\eta(x,y,t=0)$ are needed. Initialization of HOS simulation is not trivial since linear initial conditions generally do not satisfy the free surface boundary conditions. As shown by Dommermuth [16], initializing the simulation with a linear solution leads to unstable simulation, since nonlinearities do not have the time to develop before the emergence of spurious high frequency standing waves. Dommermuth developed a time relaxation scheme to avoid this problem, enabling initialisation of HOS simulation with a linear solution. This adjustment scheme smooths out the natural emergence of nonlinear terms over time by relaxing

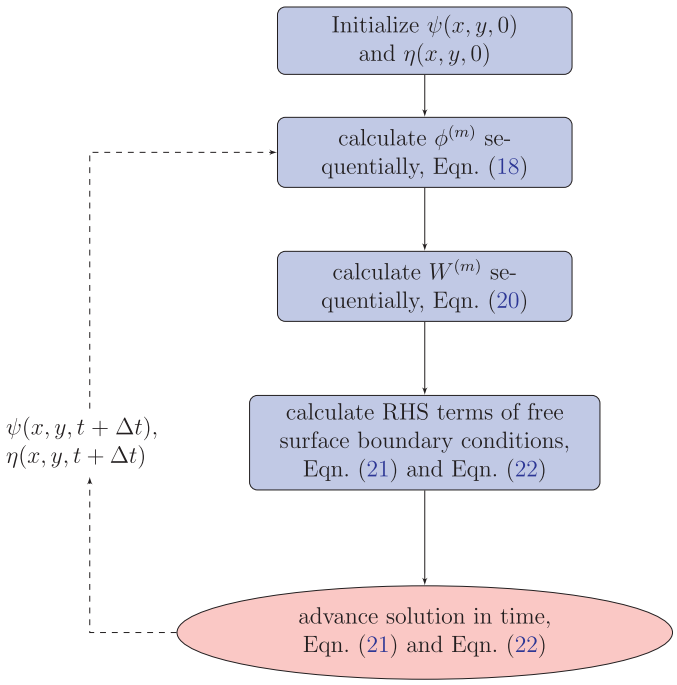


Fig. 1. Flow chart of the HOS algorithm.

the nonlinear RHS terms in free surface boundary conditions, Eqs. (4) and (5):

$$\frac{\partial \psi}{\partial t} + g\eta = G\left(1 - e^{-\left(\frac{t}{T_a}\right)^n}\right), \tag{23}$$

$$\frac{\partial \eta}{\partial t} - W^{(1)} = F\left(1 - e^{-\left(\frac{t}{T_a}\right)^n}\right), \tag{24}$$

where $T_a$ is the relaxation time, and $n$ is the relaxation exponent. According to Dommermuth [16], time relaxation period $T_a$ should be at least as long as the period of the longest wave that can occur in the simulation. $G$ and $F$ are the nonlinear parts of dynamic and kinematic free surface boundary conditions, respectively:

$$G = -\frac{1}{2}\left(\frac{\partial \psi}{\partial x}, \frac{\partial \psi}{\partial y}\right)^2 + \frac{1}{2}W^2\left(1 + \left(\frac{\partial \eta}{\partial x}, \frac{\partial \eta}{\partial y}\right)^2\right), \tag{25}$$

$$F = -W^{(1)} - \left(\frac{\partial \psi}{\partial x}, \frac{\partial \psi}{\partial y}\right)\left(\frac{\partial \eta}{\partial x}, \frac{\partial \eta}{\partial y}\right) + W\left(1 + \left(\frac{\partial \eta}{\partial x}, \frac{\partial \eta}{\partial y}\right)^2\right). \tag{26}$$

Note that linear terms are not relaxed.

### 3.4. Dealiasing

In the HOS simulation, aliasing is inevitable since multiplication of periodic fields is performed in physical space instead of spectral space [19] for the products in the free surface boundary conditions, Eqs. (4) and (5), and for the products in sequential system of equations for $\phi$ and $W$, Eqs. (14) and (15). In this work, dealiasing is performed by extending the spectra using zero-padding [19]. Zero-padding is a technique where the wave number space is extended to the size of the physical mesh and the extended part of the wave number space is set to zero. More details can be found in Canuto et al. [19]. Number of modes that may be kept in wave number space is determined using the half rule:

$$N = \frac{M+1}{2}N_{\mathscr{F}}, \tag{27}$$

where $N_{\mathscr{F}}$ is the number of modes in wave number space, while $N$ is the number of physical mesh nodes. $M$ is the nonlinearity order used in the calculation. According to Eq. (27), to maintain the same number of alias-free wave numbers $N_{\mathscr{F}}$ , for a high nonlinearity order $M$, larger physical mesh $N$ should be used. This causes the simulation to be progressively slower with increasing order of nonlinearity $M$.

### 3.5. Coupling HOS and CFD

Decomposition model [7] based on SWENSE with implicit relaxation zones and implicitly redistanced Level Set method for interface capturing is used to achieve one way coupling of HOS and CFD. HOS solution in terms of velocity and surface elevation field is imposed into the CFD domain. The surface elevation in any point in time and space is provided by direct Fourier transform:

$$\eta(x,y,t) = \sum_k \sum_l c^{\eta}_{k,l}(t) e^{iK_k ix}\, e^{iK_l y}. \tag{28}$$

The velocity field is not directly available, hence it is calculated from the velocity potential assuming the following shape function:

$$\phi(x,y,z,t) = \sum_k \sum_l c^{\psi}_{k,l}(t) \frac{\cosh\left(K_{k,l}(z+d)\right)}{\cosh(K_{k,l}d)} e^{iK_k x}\, e^{iK_l y}. \tag{29}$$

The velocity field is obtained by differentiating Eq. (29) in three Cartesian directions:

$$\begin{aligned}
v_x(x,y,z,t) &= \sum_k \sum_l c^{\psi}_{k,l}(t) iK_k \frac{\cosh\left(K_{k,l}(z'+d)\right)}{\cosh(K_{k,l}d)} e^{iK_k x}\, e^{iK_l y},\\
v_y(x,y,z,t) &= \sum_k \sum_l c^{\psi}_{k,l}(t) iK_l \frac{\cosh\left(K_{k,l}(z'+d)\right)}{\cosh(K_{k,l}d)} e^{iK_k x}\, e^{iK_l y},\\
v_z(x,y,z,t) &= \sum_k \sum_l c^{\psi}_{k,l}(t) K_{k,l} \frac{\sinh\left(K_{k,l}(z'+d)\right)}{\cosh(K_{k,l}d)} e^{iK_k x}\, e^{iK_l y},
\end{aligned} \tag{30}$$

where $z'$ stands for the vertical coordinate modified using Wheeler correction:

$$z' = qz + d(q-1), \tag{31}$$

where $q = d/(d+\eta(x,y,t))$.

### 3.6. Viscous flow model

Governing equations of the incompressible, viscous, two-phase, and turbulent flow are shown in this section.

Conservation of mass is described with the following equation:

$$\nabla \cdot \mathbf{u} = 0, \tag{32}$$

where $\mathbf{u}$ stands for a velocity field in global coordinate system. Equation of momentum conservation for a moving computational grid reads:

$$\frac{\partial \mathbf{u}}{\partial t} + \nabla \cdot ((\mathbf{u} - \mathbf{u}_M)\mathbf{u}) - \nabla \cdot (\nu_e \nabla \mathbf{u}) = -\frac{1}{\rho}\nabla p_d, \tag{33}$$

where $\mathbf{u}_M$ represents the relative grid motion velocity according to the Space Conservation Law [20], $\nu_e$ is the effective kinematic viscosity taking into account the fluid kinematic viscosity and turbulent eddy viscosity, allowing general eddy viscosity turbulence models. $\rho$ is the density field, while $pd$ stands for dynamic pressure: $p_d = p - \rho \mathbf{g}.\mathbf{x}$, where $p$ stands for total pressure, $\mathbf{g}$ is the gravitational acceleration, and $\mathbf{x}$ is the radii vector. In the present numerical model, the Ghost Fluid Method (GFM) is used to discretize free surface boundary conditions in the CFD model [21]. The GFM method takes into account the jump in density and pressure gradient on the interface, removing the spurious air velocities near the free surface. The reader is referred to Vukčević et al. [21] for more details on the GFM method.

The Level Set method is used for interface capturing with implicit redistancing [7]:

$$\frac{\partial \Psi}{\partial t} + \nabla \cdot (\mathbf{c}\Psi) - \Psi \nabla \cdot \mathbf{c} - b\nabla \cdot (\nabla \Psi) = b\frac{\sqrt{2}}{\epsilon} \tanh\left(\frac{\Psi}{\epsilon\sqrt{2}}\right), \tag{34}$$

where $\Psi$ stands for the Level Set field, while $b$ and $\epsilon$ are numerical parameters, diffusion coefficient and width parameter, respectively. $\mathbf{c}$ is the modified convective velocity. For further details regarding viscous flow model the reader is referred to Vukčević et al. [7].

## 4. Validation of the implemented HOS method

Three test cases are performed to validate the implemented HOS algorithm:

- Comparison of nonlinear monochromatic wave propagation with nonlinear analytical Stokes solution, following Dommermuth [16].
- Comparison of irregular sea state propagation with viscous, two-phase CFD study performed by Lupieri et al. [22].
- A qualitative comparison of Benjamin–Feir (BF) instability emergence with experimental results performed by Su et al. [23] and Lake et al. [24], and a quantitative comparison of induced BF instability emergence with analytic solution obtained by Stiassnie and Shemer [25].

### 4.1. Monochromatic wave train validation

Long time evolution of a progressive monochromatic wave train is conducted and compared with a nonlinear analytical Stokes solution following Dommermuth [16]. Linear solution is imposed as the initial condition from which a nonlinear solution up to 8th order is obtained.

Table 1
Comparison of HOS results and exact Stokes solution modal amplitudes.

| Order | Modal amplitude, m | | Relative error, % |
|---|---|---|---|
| | Analytical solution | HOS solution | |
| 1 | $9.9870520\times10^{-2}$ | $9.9870524\times10^{-2}$ | $4.34\times10^{-6}$ |
| 2 | $5.0594125\times10^{-3}$ | $5.0594197\times10^{-3}$ | $1.43\times10^{-4}$ |
| 3 | $3.8584235\times10^{-4}$ | $3.8584342\times10^{-4}$ | $2.78\times10^{-4}$ |
| 4 | $3.4929691\times10^{-5}$ | $3.4929838\times10^{-5}$ | $4.20\times10^{-4}$ |
| 5 | $3.4769679\times10^{-6}$ | $3.4769678\times10^{-6}$ | $-3.26\times10^{-6}$ |
| 6 | $3.6763951\times10^{-7}$ | $3.6763189\times10^{-7}$ | $-2.07\times10^{-3}$ |
| 7 | $4.0531740\times10^{-8}$ | $4.0530830\times10^{-8}$ | $-2.24\times10^{-3}$ |
| 8 | $4.6076934\times10^{-9}$ | $4.6026818\times10^{-9}$ | $-1.09\times10^{-1}$ |

Dommermuth [16] presented a HOS simulation for a wave with intermediate steepness $Ka = 0.1$, showing convergence of modal amplitudes during the simulation. In this study, the wave number is set to $K = 1$, giving the wave amplitude of $a = 0.1$ m. Relaxation time is $T_a = 8T$, where T is the wave period, and the relaxation exponent is set to $n_a = 4$.

The wave train is propagated using HOS during 100 periods, yielding 200 s of simulated time, which required 80 s of CPU time on a single core of a Intel Core i5-3570K CPU at 3.40 GHz.

Table 1 presents the comparison of HOS simulation modal amplitudes with analytical solution in terms of relative errors defined as:

$$\epsilon = (c_{kHOS} - c_{kS})/c_{kHOS}, \tag{35}$$

where $c_{kHOS}$ is the $k$th modal amplitude from the HOS simulation, while $c_{kS}$ is the $k$th modal amplitude from the analytical Stokes solution. It can be seen that the relative errors are very small, being only $4.34 \times 10^{-6}\%$ for the first order. Relative error increases for higher orders; however it remains acceptably small: the largest being $\approx 0.1\%$ for 8th order with modal amplitude of $\approx 4.6 \times 10^{-9}$ m. Order-wise rate of convergence over time is compared with the solution obtained by Dommermuth [16] in Fig. 2. The convergence rates agree well with Dommermuth's results, indicating consistent and valid implementation. It should be noted that order consistency proposed by West et al. [13] is not used here since it produced inferior results. Instead, the formulation developed by Dommermuth and Yue [12] is employed for this particular test case.

### 4.2. Propagation of unidirectional wave spectrum

Lupieri et al. [22] presented a viscous, two-phase CFD simulation of uniformly steep uni-directional spectra. Wave components are focused to create a steep focused wave, and changes in each spectrum are observed due to nonlinear and viscous effects. Focusing technique [26] is used to obtain a positive superposition of components at a desired location, and the wave energy spectrum is calculated for various locations along the basin. In HOS, FFT is performed in the spatial domain, i.e. spatial signal is transformed into wave number space. Lupieri et al. performed FFT to transform a temporal

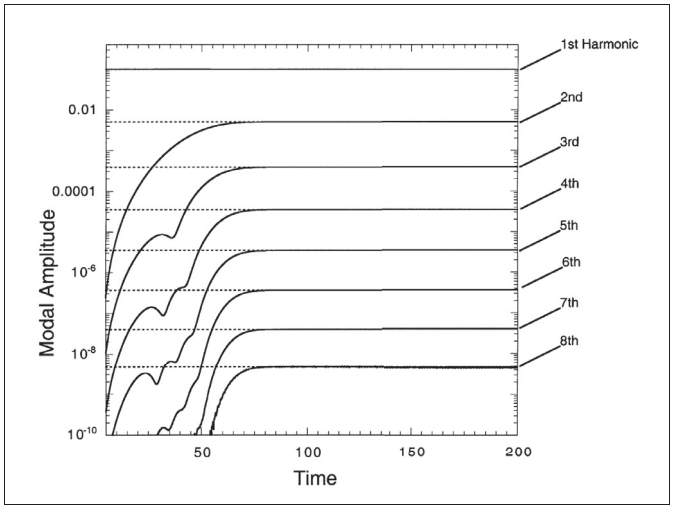


(a)

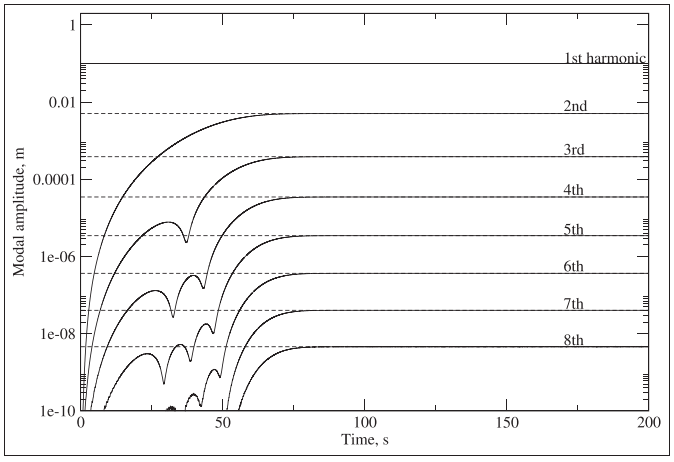


(b)

Fig. 2. Convergence rate of modal amplitudes, (a) Dommermuth [16], (b) present HOS result.

wave elevation signal into frequency domain. Although it is possible to perform a time spectral analysis of the wave elevation signal in HOS, it is not possible to achieve the same conditions of wave focusing. The reason for this is the time relaxation needed by HOS to initialize the simulation using a linear solution. As the relaxation time is several times longer than the propagation time of waves from the wave maker to the focusing location (used by Lupieri et al. [22]), HOS results are converted to the frequency domain $S_{\eta\eta}(\omega)$ from wavenumber spectrum $S_{\eta\eta}(K)$ using the dispersion relation.

Input spectra are constructed to have components with equal individual wave steepness. Four steepnesses are used: $H_i/\lambda_i = 1/715, 1/400, 1/300$ and $1/210$. Components are equidistantly spaced in the wavenumber space instead of the frequency space. Fig. 3 depicts the input spectrum with $H_i/\lambda_i = 1/715$.

For the first three cases with $H_i/\lambda_i = 1/715, 1/400, 1/300$, the spectra are calculated at $t = 37$ s while the focusing time is $T_f = 35$ s. In the case of the highest steepness $H_i/\lambda_i = 1/210$, relaxation time needs to be prolonged to $T_f = 80$ s due

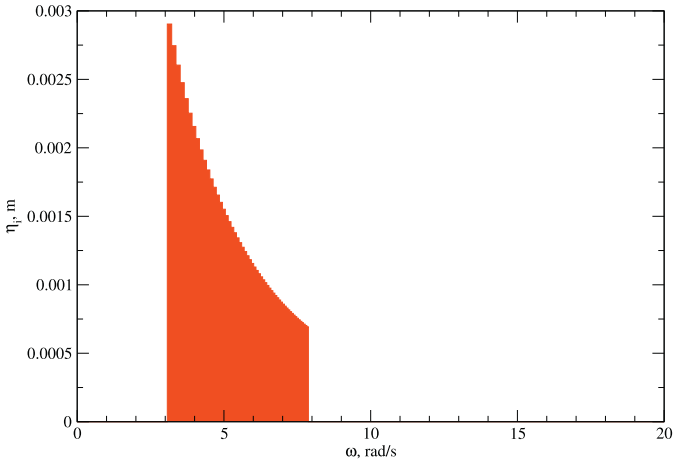


Fig. 3. Input spectrum for steepness $H_i/\lambda_i = 1/715$.

Table 2
HOS simulation parameters.

| $H_i/\lambda_i$ | 1/715 | 1/400 | 1/300 | 1/210 |
|---|---|---|---|---|
| $N_x$ | 1024 | 1024 | 1024 | 2048 |
| $M$ | 6 | 6 | 6 | 10 |
| $T_a$, s | 25 | 25 | 25 | 60 |
| $T_f$, s | 35 | 35 | 35 | 80 |

to higher nonlinearity of the spectrum, especially at focusing time. The time of focusing is increased to $T_f = 80$ s. The steeper the waves being simulated, the larger the difference between linear and non-linear solution. Thus, steeper waves demand higher relaxation time to permit stable development of the non-linear solution [16].

HOS simulation parameters are summarized in Table 2 for each test case. $N_x$ is the number of physical mesh points, $M$ is the order of nonlinearity, $T_a$ is the relaxation time, while $T_f$ is the focusing time. Following Eq. (27), number of alias-free Fourier modes corresponds to $2N_x/(M+1)$. Length of the domain used in all simulations is 72.3 m, which corresponds to 18 wave lengths of the longest input wave. For the first three cases, 1.3 s of CPU time per one second of simulated time is required, while the last case took 5 s of CPU time per second on a single core of Intel Core i5-3570K CPU at 3.40 GHz. Results are shown in Figs. 4–7.

Results shows good agreement in all test cases comparing with viscous results. Magnitude of the highest spectrum peak corresponding to $\omega \approx 3.2$ rad/s is well predicted in all test cases. Furthermore, the rightmost smaller peak at $\omega \approx 8$ rad/s is well presented. In the case of highest steepness $H_i/\lambda_i = 1/210$ two peaks are present at the rightmost of the spectrum ($6 < \omega < 8$ rad/s), and both are well predicted in HOS calculation. For the first two cases with milder steepness, shape of the spectrum in the mid frequency range ($4 < \omega < 6$ rad/s) agrees well with the viscous results. According to Lupieri et al. [22], the lower frequency peaks ($0 < \omega < 2$ rad/s) in Figs. 4(a)–7(a) correspond to second sloshing mode of the CFD basin used in their simulation. These peaks are not present in HOS simulation due to

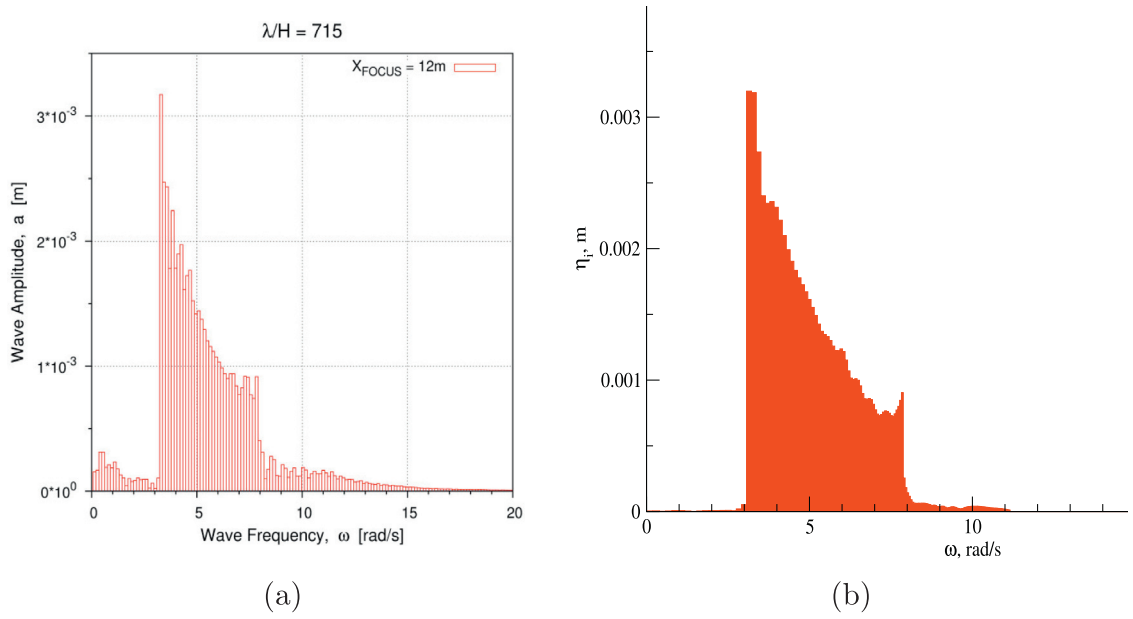


Fig. 4. Spectrum comparison for $H_i/\lambda_i = 1/715, t = 37$ s, (a) Lupieri et al. [22], (b) present result.

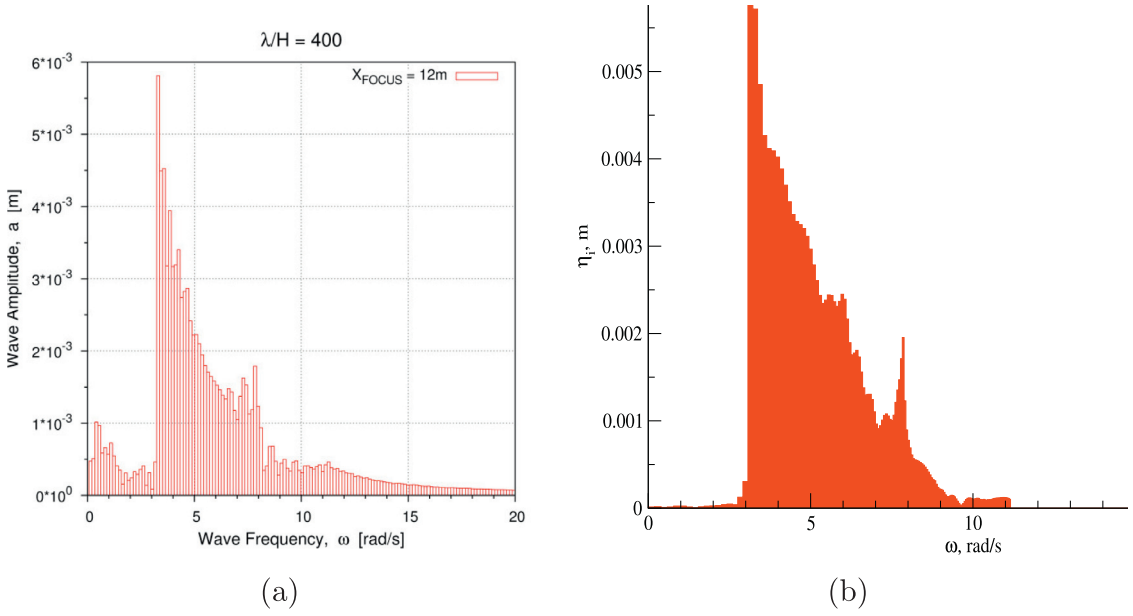


Fig. 5. Spectrum comparison for $H_i/\lambda_i = 1/400, t = 37$ s, (a) Lupieri et al. [22], (b) present result.

unbounded periodic wave propagation. The cases for steepness $H_i/\lambda_i = 1/300$ and 1/210 correspond to wave breaking events at the focusing time, causing larger discrepancies in the mid frequency range ($4 < \omega < 6$ rad/s), which increase for larger steepness. HOS method is not able to capture wave braking events since $\eta$ is a single valued function. When $\eta$ has more than one solution (multi-valued function), the failure of convergence is caused by spurious high wave number components, which are truncated via filtering. In Figs. 4(b)–7(b), it can be seen that the frequency range is truncated at approximately 11 rad/s. This truncation enables HOS simulation to continue beyond the breaking event, causing energy loss. This is shown in Fig. 8, where computed energy over time is compared with the initial energy of the linear spectrum. This energy loss is present in the viscous study as well, however it is caused mainly by viscous dissipation in wave breaking mechanism. As expected, cases that correspond to wave braking events show larger energy loss after the focusing time.

### 4.3. Development of Benjamin–Feir instabilities

In their study, Benjamin and Feir [17] discovered an instability that occurs in monochromatic wave train. The instability was confirmed by numerous experiments, Feir [27] being the first. As shown by McLean et al. [28] and McLean [29],

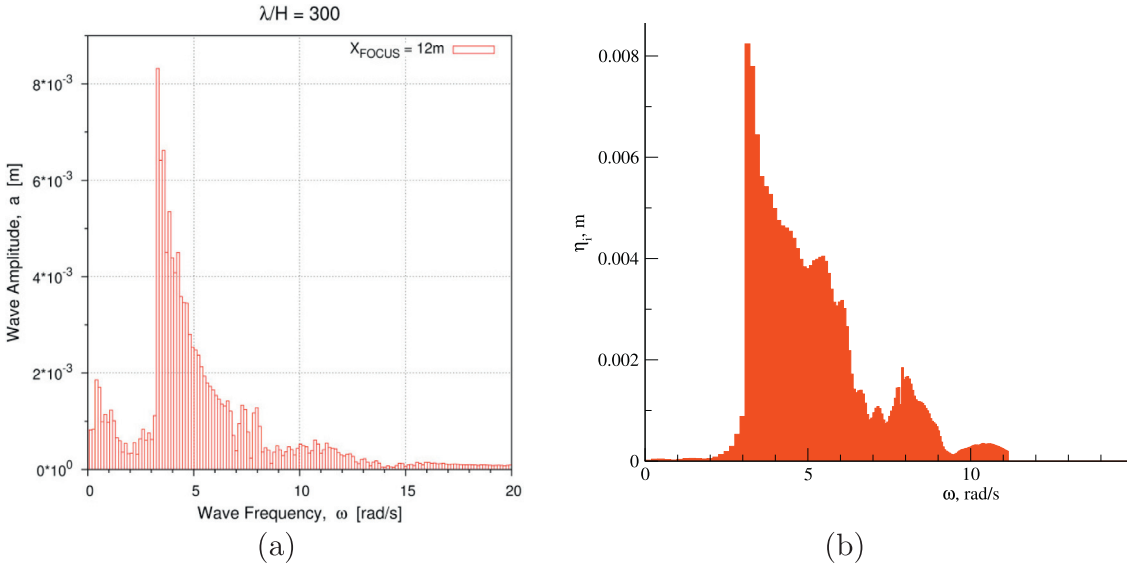


Fig. 6. Spectrum comparison for $H_i/\lambda_i = 1/300, t = 37$ s, (a) Lupieri et al. [22], (b) present result.

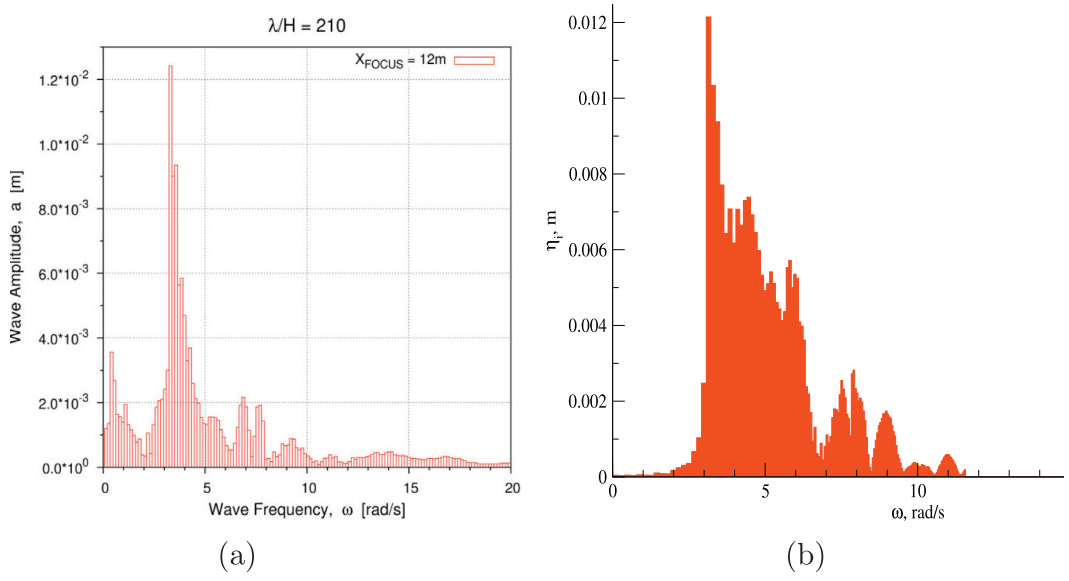


Fig. 7. Spectrum comparison for $H_i/\lambda_i = 1/210, t = 84$ s, (a) Lupieri et al. [22], (b) present result.

there are two main types of instabilities in wave trains. Type I is the Benjamin–Feir instability, which occurs for waves of steepness $Ka < 0.38$, while type II occurs for $Ka > 0.4$. Only Benjamin–Feir instabilities will be considered in this section, which manifest as the emergence of nonlinear side bands whose amplitudes grow exponentially once they emerge. Side bands emerge near the carrier frequency and near higher order modes. The growth is initialized by an initial disturbance which is always present in nature and in numerical simulation (due to numerical errors), or it can be imposed. The growth of nonlinear sidebands occurring in HOS simulation is compared with theory and experiment.

First, a qualitative comparison is performed where the natural growth is observed, i.e. there is no imposed initial disturbance. Wave parameters used in the simulation and the HOS parameters are given in Table 3. HOS simulation is initialized using a linear solution. Simulation required ≈2 s of CPU time per one second of simulated time on a single core of Intel Core i5-3570K CPU at 3.40 GHz.

Time evolution of nonlinear side-bands in frequency domain is given in Fig. 9, and the dispersion relation is used to transform from the wave number to the frequency domain. Time domain Fourier analysis is difficult in HOS simulation since the occurrence of Benjamin–Feir instabilities is transient in time, and cannot be captured accurately by performing Fourier transform on the time elevation signal. The nonlinearities in HOS simulation evolve in time in the whole spatial domain, while in the experiment, nonlinearities evolve with waves propagating in space. A probe measuring elevation over time in the experiment will always be exposed to the

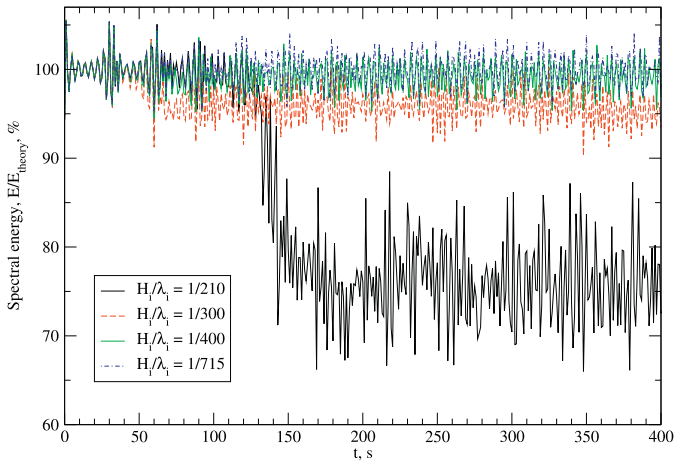


Fig. 8. Spectral energy computed in space during simulated time window.

Table 3
Wave and HOS simulation parameters.

| $Ka$ | $K$, rad/m | $T$, s | $T_a$, s | $n_a$ | $M$ | $N_x$ |
|---|---|---|---|---|---|---|
| 0.25 | 16.1 | 0.5 | 5 | 4 | 8 | 1024 |

same level of nonlinearity, since it is always equally distanced from the wave maker. This allows a time Fourier transform which produces spectrum in the frequency domain. Fig. 10(a) and (b) presents spectra for the corresponding wave steepness from the experimental studies of Su et al. [23] and Lake et al. [24], respectively.

According to Benjamin and Feir [17], the strongest instability growth is for $\delta = Ka$ where $\delta = \Delta f/f$. $\Delta f$ is the frequency separation of the carrier frequency $f$ and the frequencies of the higher and lower nonlinear side bands. It can be seen in Fig. 9 that the frequencies of the nonlinear side bands near the carrier frequency are approximately 9.7 and 14.8 rad/s. The carrier frequency is $\omega = 12.56$ rad/s which gives $\Delta\omega = 3.14$ rad/s. The frequencies of the fastest growing side bands are expected to be 9.4 and 15.7 rad/s, which is close to the obtained values. Part of the difference is caused by the use of linear dispersion relation.

A quantitative comparison is performed for a case where the initial instabilities are imposed. Following Stiassnie and Shemer [25] the initial solution comprises carrier Airy wave with $kA = 0.13$ and two sidebands harmonics with amplitudes 10% of the carrier wave, with $\pm 22\%$ wavenumber separation in respect to the carrier wave. Following Dommermuth and Yue [12] the carrier wavenumber is set to $K_c = 9$ rad/m to allow integral wavenumbers of sidebands; for the subharmonic $K_- = 7$ rad/m and for the superharmonic $K_+ = 11$ rad/m. In HOS simulation the order of nonlinearity is set to $M = 4$, while the number of grid points is $N = 128$. Time relaxation and order consistency are not used.

Time histories of the three harmonics obtained with HOS and by Stiassnie and Shemer are presented in Fig. 11, where $\eta/\eta_0$ is the wave amplitude normalised by carrier wave amplitude, and $t/T_0$ is the time scaled with carrier wave period. It can be seen that evolution of individual harmonics agrees well with the analytical solution. HOS simulation predicts the first minimum of the carrier mode near $t \approx 80T$, while the analytical solution predicts $t \approx 60T$. However, the distance between carrier mode minima is $\approx 85T$ for both HOS simulation and the analytical solution. It can be concluded that there is a delay in the nonlinearity development at the beginning of the simulation, but the time scale of nonlinear behaviour is well predicted.

## 5. Validation of coupling HOS and CFD

The coupling between HOS and CFD described in Section 3.6 is validated on a three hour irregular wave propagation. The validation is performed by comparing the wave energy spectrum obtained from HOS with the spectrum obtained in CFD measured at the same location. HOS simulation is initialised using JOSWAP spectrum with $H_s = 17$ m, $T_p = 15.5$ s and $\gamma = 2.6$. In the HOS simulation, $M = 3$ is used, $N_x = 2048$, and domain length is $L_x = 60,000$ m. Two-dimensional CFD simulation is carried out with domain 2160 m long, 100 m deep and 40 m high (above the calm free surface). Near the free surface the cells have the size of $0.5 \times 0.5$ m, while the grid counts 136,800 cells. Fixed time step of $\Delta t = 0.31$ s is used which corresponds to 50 time-steps per peak period of the spectrum. Inlet relaxation zone is 700 m long, while the outlet is 1000 m long, leaving 460 m of unaffected CFD domain. Long relaxation zones are necessary in order to prevent the reflection of the longest waves that can occur in the sea state, and to prevent standing waves corresponding to the natural frequency of the numerical wave tank. Given the small depth of the domain, the velocity field from HOS solution is imposed to the bottom boundary in order to mimic the rest of the fluid below the level of the bottom boundary. Fig. 12 shows the volume fraction field reconstructed from the level set variable in one time instant. The free surface is well preserved with very little smearing. The waves propagate from left to right.

As in the experimental wave basin test, the initial linear spectrum needs to be calibrated in order to obtain the imposed JONSWAP spectrum in the HOS realisation. Calibration of the initial HOS condition is performed by running at least ten three hour realisations of the target spectrum, and acquiring the average correction factors for the initial linear spectrum. In Fig. 13 the target spectrum is compared to the spectrum obtained before and after calibration.

The calibration coefficients are applied to the linear JONSWAP spectrum with random phase shifts used to initialise the HOS simulation coupled to the CFD simulation. Fig. 14 shows the comparison of wave energy spectrum obtained from the HOS simulation, and the spectrum measured in the corresponding CFD simulation. The damping of spectral wave energy is minimal, and the spectrum shape corresponds well. The agreement is better for lower frequencies, while higher frequencies ($\omega > 0.6$ rad/s) exhibit larger relative damping, which is caused by smaller spatial and temporal resolution relative to wave component height, length and period. In

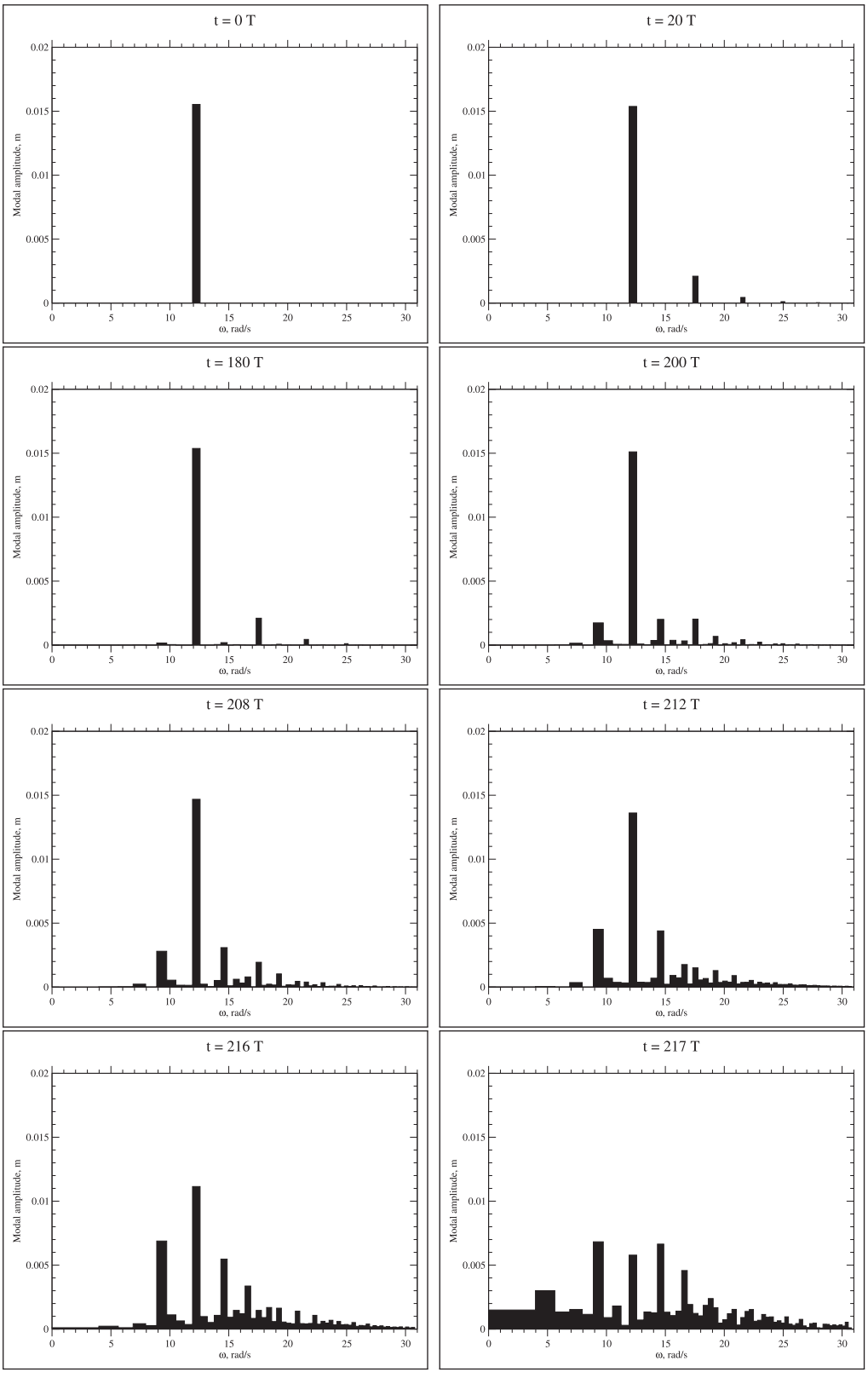


Fig. 9. Development of nonlinear side bands in HOS simulation.

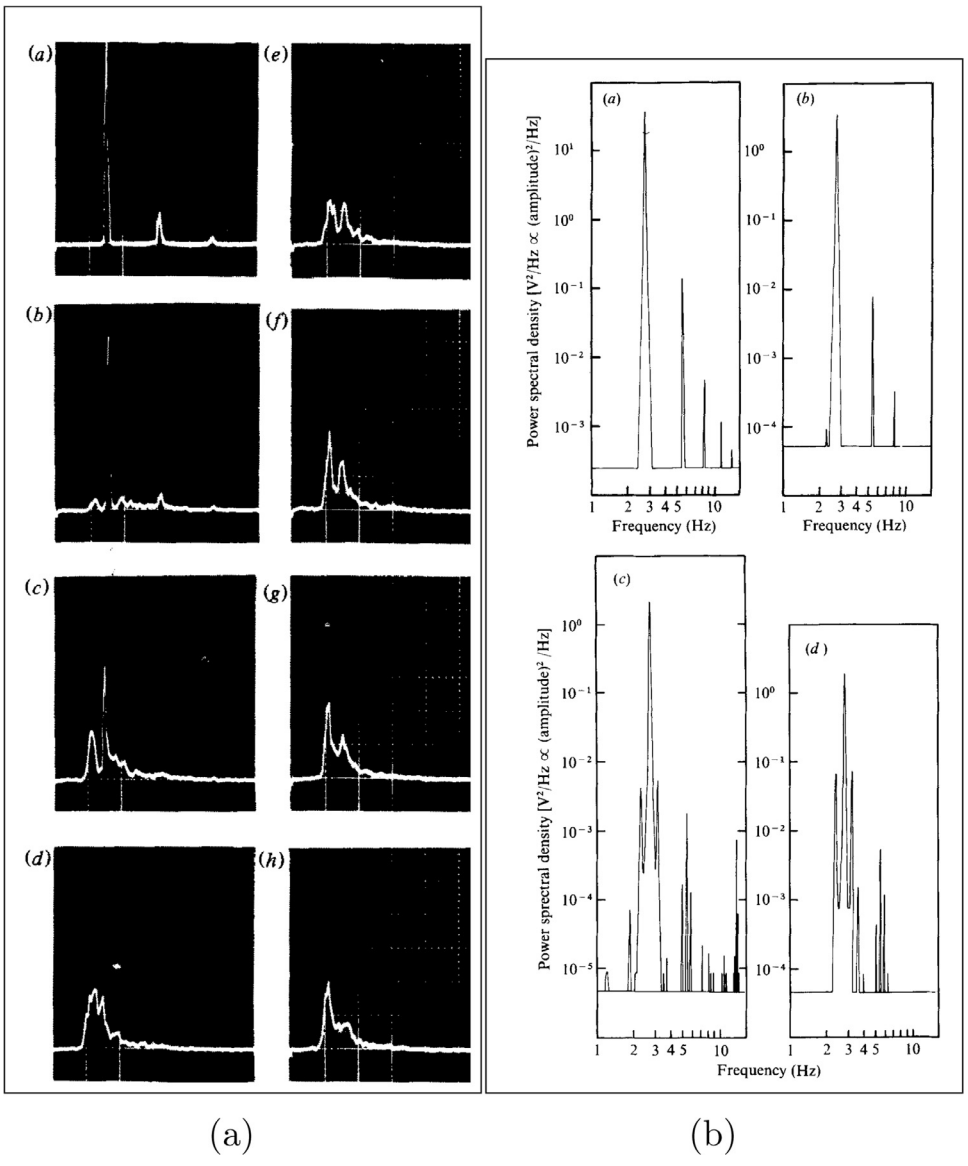


Fig. 10. Experimental nonlinear side bands development, (a) Su et al. [23], (b) Lake et al. [24].

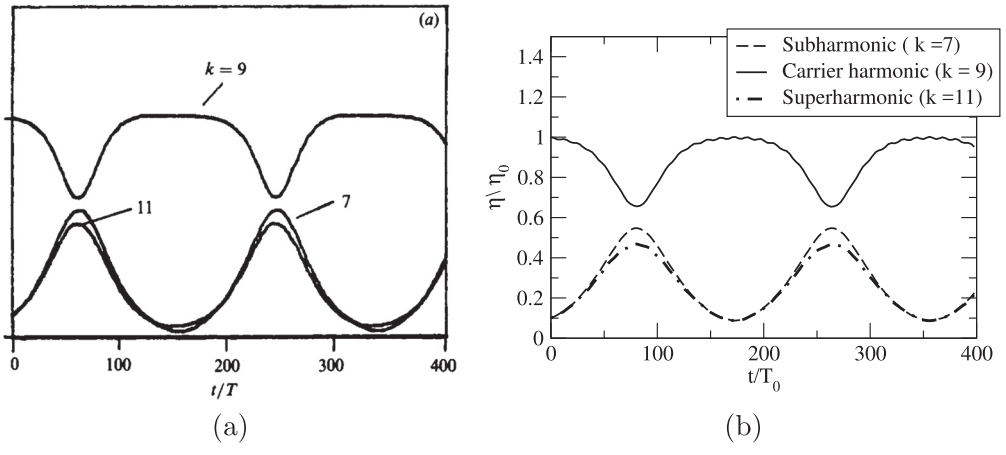


Fig. 11. Time histories of the carrier, subharmonic and superharmonic wave amplitudes, (a) analytic solution by Stiassnie and Shemer [25], (b) present result.

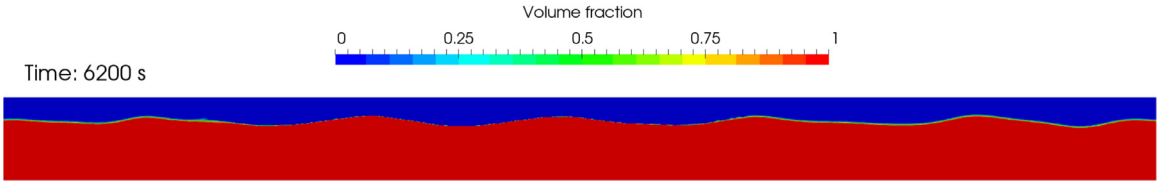


Fig. 12. Snapshot from the irregular wave propagation CFD simulation.

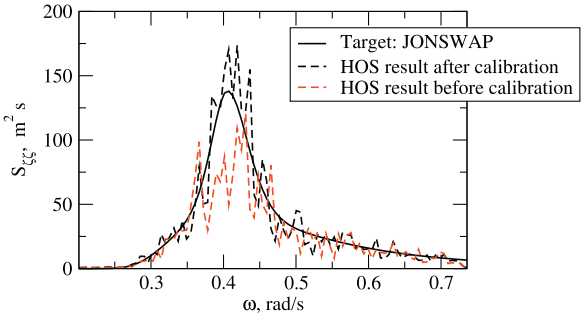


Fig. 13. Comparison of wave energy spectrum obtained with HOS before and after calibration.

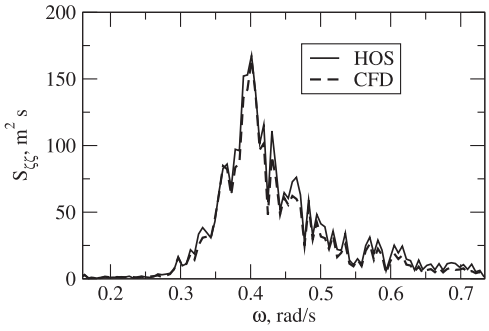


Fig. 14. Comparison of wave energy spectrum obtained with HOS and CFD.

Table 4
Quantitative comparison of wave energy spectrum obtained with HOS and CFD.

| | $H_s$, m | $T_p$, s |
|---|---|---|
| HOS | 17.12 | 12.76 |
| CFD | 16.13 | 13.11 |

Table 4 the two spectra are compared quantitatively, where $H_s$ and $T_p$ are compared. The significant wave height corresponds quite well, where damping in CFD results in 1 m smaller height corresponding to 5.8% difference. For the peak period the difference is smaller, being less than 2%. Note that the peak period differs significantly with respect to the theoretical value of 15.5 s. This is caused by the fact that the spectrum used in HOS is truncated for stability reasons, hence the theoretical expression for the peak period calculation derived based on the wave elevation distribution is not valid, however it enables a quantitative comparison.

## 6. CFD simulation of a 3D extreme wave encountering a full scale container ship

In this section a simulation of a 3D extreme wave encountering a freely floating full-scale container ship is presented. The hull form parameters of the KRISO Container Ship (KCS) are available at the Tokyo Workshop on CFD in Ship Hydrodynamics [30].

Unstructured grid with 1.2 million cells is used, mostly composed out of hexahedral cells (≈83%), the rest being polyhedral cells. At the hull surface, the grid is aligned with the hull surface with boundary layer refinement. The transition from the boundary layer cells to the surrounding background orthogonal grid is accomplished with polyhedral cells. Second order backward scheme is used for temporal discretisation in the momentum equation, while implicit first order upwind scheme is used for convection with second order, upwind biased deferred correction. Second order scheme with explicit limited non-orthogonal correction is used for the discretisation of the Laplace operator for the diffusion term in the momentum equation and the pressure. No turbulence modelling is used in this case since the ship has zero initial velocity, hence adverse pressure gradients can be expected near the hull in the wave field, rendering conventional eddy viscosity turbulence models non-valid.

A 3D extreme wave is obtained using HOS, where the HOS simulation is initialized using a linear directional spectrum. Directional spreading is modelled using the following expression [31]:

$$D(\theta) = \begin{cases} A(n)\cos^n\theta & \text{for } |\theta| \le \pi/2, \\ 0 & \text{for } |\theta| > \pi/2, \end{cases} \tag{36}$$

where $A(n)$ is the normalisation coefficient, $\theta$ is the dominant wave propagation direction, and $n$ is the arbitrary directionality parameter. As the initial condition for HOS simulation, JONSWAP spectrum is used with significant wave height $H_s = 10.5$ m, peak period $T_p = 9.5$ s, and directionality constant $n = 8$. Dominant wave propagation direction is set to $\theta = 25^\circ$ with respect to longitudinal ship axis. Extreme wave occurred after $\approx 56T_p$ with wave height $H = 21.91$ m, as it can be seen on Fig. 15 at approximately $x = 900$ m and $y = 200$ m.

30 s of simulation took 132 h of CPU time on a Intel Core i7-4820K CPU at 3.70 GHz. Fig. 16 sequentially shows the encounter of the extreme wave on the KCS. At time zero, CFD simulation is initialized with the HOS solution corresponding to time $T_{HOS} = 526$ s. HOS simulation is then ran alongside the CFD simulation to produce the necessary

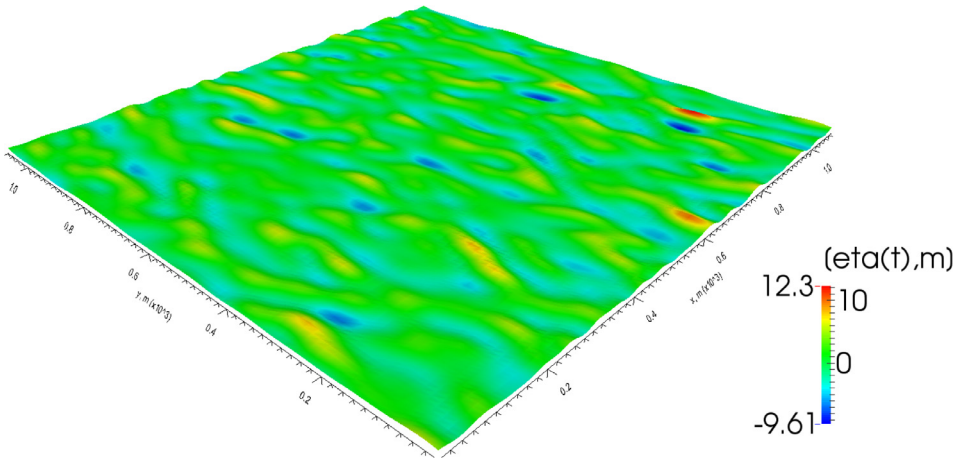


Fig. 15. Free surface elevation with freak wave event, $t = 532$ s.

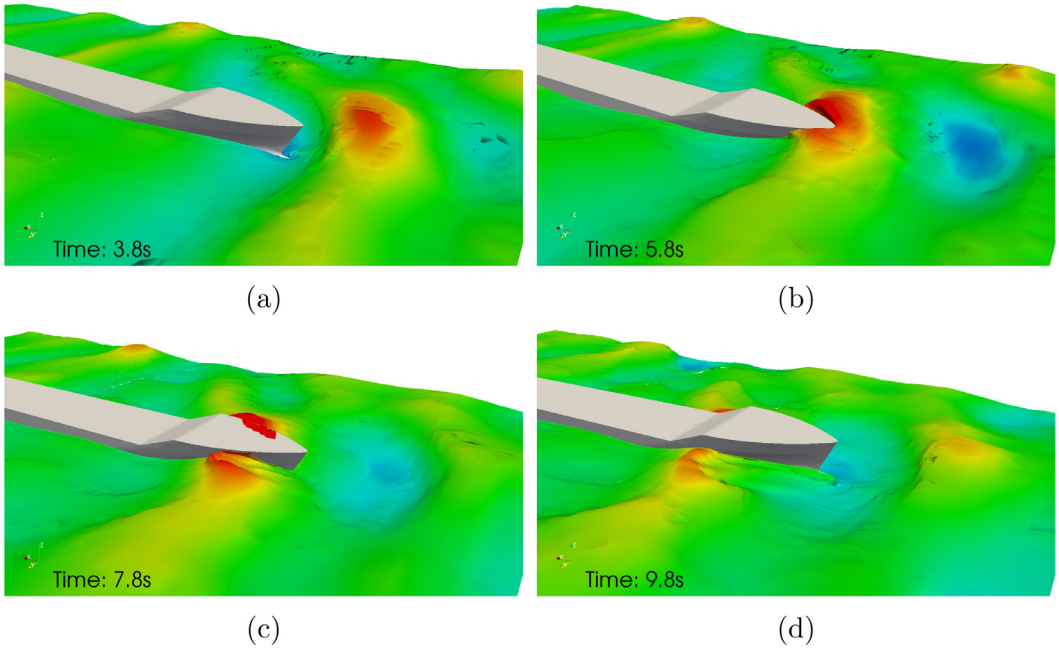


Fig. 16. Three-dimensional freak wave encountering a full scale KCS. (The colour legend in this figure corresponds to Fig. 15).

blending results at the required time instances. At CFD simulation time $T = 5.8$ s the extreme wave encounters the bow of the container ship, while the green water event can be seen after the impact at $T = 7.8$ s. Fig. 17 shows the translational motion of the ship's centre of gravity during the simulation. It can be noticed that sway motion is greater than surge motion, due to the angle of dominant wave propagation direction. On Fig. 18 the rotation of the ship is shown, where significant roll angle can be seen.

Unfortunately, neither experimental nor numerical data are available for comparison today.

## 7. Summary

In this paper a framework for efficient irregular wave simulation using HOS and CFD coupling is presented. HOS is a pseudo-spectral, potential flow method for solving nonlinear free surface boundary conditions. It is primarily used to propagate arbitrary wave energy spectra, taking into account nonlinear wave-to-wave interaction and wave modulation. Among other applications, HOS can be used for low CPU cost extreme wave initialization for fully non-linear CFD simulations of wave impact and wave breaking.

The accuracy and validity of the implemented HOS model is assessed with three validation test cases. In the first test case, HOS solution of a propagating monochromatic wave train is considered, where modal amplitudes up to 8th order compare well with the analytical Stokes solution. The comparison verifies that given a linear initial condition, HOS can evolve the nonlinear solution accurately. Rate of convergence is also compared and shows good agreement with results obtained by Dommermuth [16].

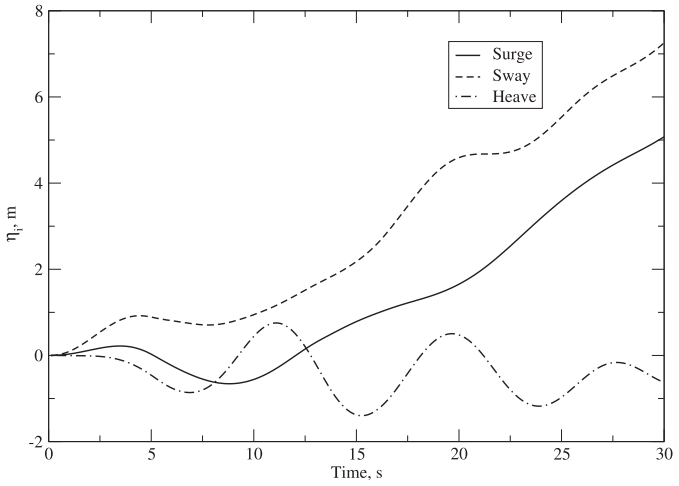


Fig. 17. Translational motion of the ship's centre of gravity during the extreme wave impact.

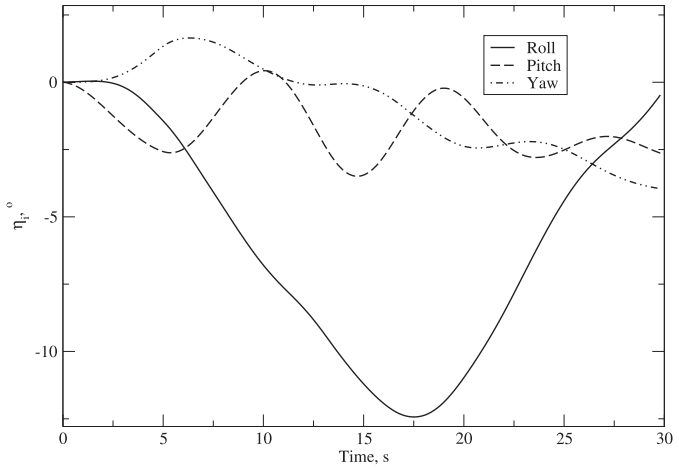


Fig. 18. Rotational motion of the ship around the centre of gravity during the extreme wave impact.

The second test case presents the propagation of four different uniformly steep, uni-directional input spectra where the solutions are compared with the viscous study performed by Lupieri et al. [22]. Results show good agreement, especially for wave spectra with smaller steepness.

The final validation case simulates the occurrence of Benjamin–Feir type instability in a propagating monochromatic wave train. Benjamin-Feir instability produced by HOS method agrees well with experimental and theoretical studies.

In order to test the precision of the HOS–CFD coupling, energy wave spectra obtained in HOS and corresponding CFD simulation is compared. The two spectra correspond well, indicating minor damping of wave energy.

Finally, an example CFD simulation is shown where the coupling of HOS and CFD is used to simulate a 3D directional extreme wave encountering a full-scale, freely floating container ship.

In future efforts the presented coupling will be utilised in order to calculate extreme response of naval objects such as green water, slamming and motion.

## References

[1] W.R. Van Dalsem, J.L. Steger, in: Proceedings of AGARD Fluid Dynamics Panel Symposium on Application of CFD in Aeronautics, 1986.
[2] N.G. Jacobsen, D.R. Fuhrman, J. Fredsøe, Int. J. Numer. Methods Fluids 70 (9) (2012) 1073–1088, doi:10.1002/fld.2726.
[3] B.T. Paulsen, H. Bredmose, H.B. Bingham, Coast. Eng. 86 (2014) 57–76, doi:10.1016/j.coastaleng.2014.01.006.
[4] A.P. Engsig-Karup, H.B. Bingham, O. Lindberg, J. Comput. Phys. 228 (2009) 2100–2118, doi:10.1016/j.jcp.2008.11.028.
[5] B.T. Paulsen, H. Bredmose, H.B. Bingham, N.G. Jacobsen, J. Fluid Mech. 755 (2014) 1–3, doi:10.1017/jfm.2014.386.
[6] A. Pistidda, H. Ottens, in: Proceedings of the 18th Numerical Towing Tank Symposium, 2015, pp. 161–166.
[7] V. Vukčević, H. Jasak, S. Malenica, Ocean Eng. 121 (2016) 37–46, doi:10.1016/j.oceaneng.2016.05.022.
[8] P. Ferrant, L. Gentaz, D. Le Touzé, in: Proceedings of Numerical Towing Tank Symposium, NuTTS, 2002.
[9] C. Monroy, G. Ducrozet, A. Bonnefoy, A. Babarit, P. Ferrant, in: Proceedings of the 20th International Off-shore and Polar Engineering Conference, 2010, pp. 678–685.
[10] R. Marcer, C. Audiffren, C. Dassibat, C. de Jouette, P.E. Guillerm, in: Proccedings of 11éme Journées de l'Hydrodynamique, 2007, pp. 1–12.
[11] C. Kharif, E. Pelinovsky, Eur. J. Mech. B: Fluids 22 (2003) 603–634.
[12] D.G. Dommermuth, D.K.P. Yue, J. Fluid Mech. 184 (1987) 267–288.
[13] B.J. West, K.A. Brueckner, R.S. Janda, J. Geophys. Res. 92 (C11) (1987) 11803–11824.
[14] M. Tanaka, Fluid Dyn. Res. 28 (2001) 41–60.
[15] G. Ducrozet, F. Bonnefoy, D. Le Touzé, P. Ferrant, Nat. Hazards Earth Syst. Sci. 7 (2007) 109–122.
[16] D.G. Dommermuth, Wave Motion 32 (2000) 307–317.
[17] T. Benjamin, J.E. Feir, J. Fluid Mech. 27 (1967) 417–430.
[18] W.H. Press, S.A. Teukolsky, W.T. Vetterling, B.P. Flannery, Numerical Recipes in C++: The Art of Scientific Computing, Cambridge University Press, 2002.
[19] C. Canuto, M. Hussaini, A. Quarteroni, T. Zang, Spectral Methods in Fluid Dynamics, Springer, 1988.
[20] I. Demiridžić, M. Perić, Int. J. Numer. Methods Fluids 8 (1988) 1037–1050, doi:10.1002/fld.1650080906.
[21] V. Vukčević, H. Jasak, I. Gatin, Comput. Fluids 153 (2017) 1–19.
[22] G. Lupieri, T. Puzzer, G. Contento, in: Proceedings of the 21th Symposium Sorta, 2014.
[23] M. Su, M. Bergin, P. Marler, R. Myrick, J. Fluid Mech. 124 (1982) 45–72.
[24] B.M. Lake, H.C. Yuen, H. Rungaldier, W.E. Ferguson, J. Fluid Mech. 83 (1977) 49–74.
[25] M. Stiassnie, L. Shemer, J. Fluid Mech. 174 (1987) 299–312.
[26] J.R. Chaplin, Int. J. Offshore Polar Eng. 6 (2) (1996) 131–137.
[27] J.E. Feir, Proc. Roy. Soc. Lond. A 299 (1967) 54–58.
[28] J.W. McLean, Y. Ma, D. Martin, P. Saffman, H. Yuen, Phys. Rev. Lett. 46 (1981) 817–820.
[29] J.W. McLean, J. Fluid Mech. 114 (1982) 315–330.
[30] National Maritime Reasearch Inistitute (NMRI), in: Proceedings of Tokyo 2015: A Workshop on CFD in Ship Hydrodynamics, 2015. http://www.t2015.nmri.go.jp/ (Online; accessed 20.08.15).
[31] L.H. Holthuijsen, Waves in Oceanic and Costal Waters, Delft University of Techonlogy and UNESCO-IHE, 2007.